

UNIVERSITY of CALIFORNIA  
SANTA CRUZ

**THE USE OF PHOTOMULTIPLIER TUBES IN GAMMA-RAY  
ASTRONOMY**

A thesis submitted in partial satisfaction of the  
requirements for the degree of

BACHELOR OF SCIENCE

in

PHYSICS

by

**Douglas Long**

June 1 2011

The thesis of Douglas Long is approved by:

---

Professor David Williams  
Advisor

---

Dr Adriane Steinacker  
Theses Coordinator

---

Professor David P. Belanger  
Chair, Department of Physics

Copyright © by

Douglas Long

2011

## **Abstract**

The Use of Photomultiplier Tubes in Gamma-Ray Astronomy

by

Douglas Long

The Hamamatsu H8500 -103 MOD8 multianode photomultiplier was tested for use in the upcoming telescope arrays for the CTA collaboration. The characteristics of interest are the gain uniformity, afterpulsing rates and photon detection efficiencies. A 4 channel, 10 gigasample/sec waveform sampler was used to measure the gain and a CAMAC system was used to measure the afterpulsing rates and photon detection efficiency. The gain uniformity was found to be acceptable; the mean was found to be  $1.8 \times 10^5$  at 890V with an RMS of  $2.6 \times 10^4$ . The afterpulsing rates was also found to be below the required rate of  $1 \times 10^{-3}$  in most pixels. The few pixels that showed higher afterpulsing rates were pixels on the edge of the tube and the results require further testing to verify the higher rates are not spurious. The photodetection efficiency was found to be a disappointment, but at this point the H10966 is still the best option. Further modifications and testing is needed before a decision can be made.

# Contents

<b>List of Figures</b>	<b>vi</b>
<b>List of Tables</b>	<b>vii</b>
<b>Acknowledgments</b>	<b>viii</b>
<b>1 Introduction</b>	<b>1</b>
1.1 History of Gamma-Ray Astronomy . . . . .	1
1.2 Ground Based Detection and Particle Showers . . . . .	2
1.3 Imaging Atmospheric-Cherenkov Telescope . . . . .	4
1.4 Purpose of the Research . . . . .	6
<b>2 Experimental Set-up and Equipment</b>	<b>7</b>
2.1 Photomultiplier Tubes . . . . .	7
2.1.1 Hamamatsu H8500D-103 MOD 8 . . . . .	9
2.2 Electronics and Data Acquisition . . . . .	10
2.2.1 Amplification . . . . .	10
2.2.2 DRS4 Evaluation Board . . . . .	11
2.2.3 CAMAC . . . . .	11
<b>3 Experimental Procedure and Software</b>	<b>12</b>
3.1 Gain Measurement . . . . .	12
3.1.1 Procedure . . . . .	13
3.1.2 Software . . . . .	14
3.2 Afterpulsing Measurements . . . . .	17
3.2.1 Procedure . . . . .	18
3.2.2 Software . . . . .	19
3.3 An Alternate Afterpulsing Method . . . . .	20
3.4 Photon Detection Efficiency . . . . .	23
3.4.1 Procedure . . . . .	24
3.4.2 Software . . . . .	26
<b>4 Analysis and Results</b>	<b>28</b>
4.1 Results of Gain Measurements . . . . .	28
4.2 Results of Afterpulsing Measurements . . . . .	31
4.3 Results of Photon Detection Efficiency Measurements . . . . .	34

<b>5 Discussion</b>	<b>36</b>
5.1 Broad Single Photoelectron Distribution . . . . .	36
5.2 Decrease in Gain at High Light Levels . . . . .	37
5.3 Conclusion . . . . .	39
<b>Bibliography</b>	<b>40</b>

# List of Figures

1.1	Pair Production, <i>electrons.wikidot.com</i> . . . . .	3
1.2	Bremsstrahlung Radiation, <i>www.dur.ac.uk</i> . . . . .	4
1.3	Simulations of two Air Cherenkov shower (Left: gamma-ray initiated. Right: Nucleon initiated). The black tracks shows the trajectory of the showers. The horizontal axis shows the spread with respect to the shower axis. <i>imagine.gsfc.nasa.gov</i> . . . . .	5
2.1	Cross section of a photomultiplier tube, <i>http://micro.magnet.fsu.edu</i> . . . . .	8
2.2	Band model for semiconductors[5]. . . . .	9
2.3	Hamamatsu H8500D-103 MOD 8. <i>http://sales.hamamatsu.com</i> . . . . .	10
3.1	Circuit diagram used in the gain measurements. . . . .	14
3.2	Graphical user interface used to control the DRS . . . . .	15
3.3	Circuit diagram used in the rate vs threshold measurements. . . . .	20
3.4	Circuit diagram used in the DRS afterpulsing measurements. . . . .	21
3.5	Two histograms output by the DRS analysis for afterpulsing. On the left, the time between the initial signal and the afterpulse is shown and on the right, the distribution of single PE amplitudes is shown. . . . .	22
3.6	A 2D histogram showing the time and amplitude of all afterpulses found. . . . .	23
3.7	LED set-up used to measure photodection efficiency . . . . .	25
4.1	Typical average pulse shape for the Hamamatsu H8500D.(pixel 4) . . . . .	29
4.2	Single-photoelectron amplitude distribution for the Hamamatsu H8500D. (pixel 4) . . . . .	29
4.3	Distribution of gains measured for all 64 pixels. . . . .	30
4.4	Rate vs threshold curve measured in a completely dark environment for pixel 4 . . . . .	31
4.5	Rate vs threshold curve measured with a steady LED for pixel 4 . . . . .	32
4.6	Rate vs threshold curve with the thermionic noise subtracted out for pixel 4 . . . . .	32
4.7	Rate vs threshold curve with the thermionic noise subtracted out for pixel 8, a corner pixel . . . . .	34
4.8	Quantum efficiency of three types of photocathodes[6]. . . . .	35
5.1	Width of the distribution, relative to the single photoelectron amplitude vs gain. . . . .	37
5.2	Gain of pixel 45 at various background light levels . . . . .	38

# List of Tables

1.1	Gamma-ray bands and the detection method [11]. . . . .	2
4.1	Uniformity of the gain rate across the 64 channels. . . . .	30
4.2	Afterpulsing rate of the 64 channels. Pixel one is represented by the top left corner. . . . .	33
4.3	Photon detection efficiency for various pixels of the H8500D-103 MOD8 . . . . .	35

## **Acknowledgments**

I wish to thank all those who encouraged and helped me. Without them, I could not have completed this project.

David Williams: For giving me the opportunity to research and for providing aid and support for this thesis.

Nepomuk Otte: For sharing his expertise and aiding with the programming for this thesis.

Adriane Steinacker: For her invaluable feedback.



# 1 Introduction

This thesis includes a discussion of the history of gamma-ray astronomy and a detailed discussion of the research on photomultiplier tubes to be use in the AGIS observatory. Background information on gamma-ray astronomy and the observatory will be presented first, followed by discussions of the equipment, procedures and results.

## 1.1 History of Gamma-Ray Astronomy

Our knowledge of the physical universe is almost entirely due to observing electromagnetic radiation. Prior to WWII, astronomy was limited to observing only the visible spectrum. During the Second World War, radar technology was produced that would later lay the foundation for radio astronomy. Later, rocket technology formed the basis for x-ray astronomy[11]. As technology grew more sophisticated, astronomers were able to study radiation further away from the visible band. This paper will focus on the highest end of the spectrum, gamma rays. Gamma-rays can be used to observe the most energetic objects in the universe such as supermassive black holes. Gamma-ray astronomy also has the unique ability to study dark matter [1].

In 1949, the neutral pion was discovered and three years later Hayakawa predicted that gamma ray emission from the decay of neutral pions occur when cosmic rays interact with interstellar matter [2]. Shortly thereafter, Hutchinson theorized that gamma-rays are emitted from cosmic bremsstrahlung. The concept of gamma-ray astronomy was first introduced in by Phillip Morrison's 1958 seminal paper, where he made estimates of gamma ray fluxes for several astronomical bodies

Band Range Environment	Low/Medium 0.1-30 MeV Space	High 30 MeV - 100 GeV Space/Ground	Very High 100 GeV - 100 TeV Ground	Ultra High >100 TeV Ground
------------------------------	-----------------------------------	--	--	----------------------------------

Table 1.1: Gamma-ray bands and the detection method [11].

[9]. At this point, gamma ray detectors were already developed, but due to the high energy, detection proved to be more difficult than initially expected. Unlike radiation in the visible band, the earth's atmosphere is not transparent to gamma rays, limiting their direct detection to experiments mounted on high altitude balloons or satellites. The first balloon experiments in the 1950s failed to detect gamma rays because they could not fly high enough to filter out the atmospheric gamma-rays that hampered the detection of the primary radiation. During the Cold War, satellite launches made satellite-based detectors feasible. Detectors on board the Explorer 11 satellite made the first reliable gamma ray detections [2]. However, due to weight and volume limitations, only gamma rays with energy up to 300GeV can be detected. To observe higher energy gamma rays indirect methods of detection must be used. Table 1.1 shows energy bands of gamma-rays. Gamma-rays with energy less than about 100 GeV do not have sufficient energy to be detected by indirect methods. however recent advancements are allowing indirect methods to work at lower energies.

## 1.2 Ground Based Detection and Particle Showers

Shortly after the publication of Morrisons paper, a high energy theorist at CERN, Giuseppe Cocconi, predicted that gamma-rays with energies greater than 100GeV could be used to observe the universe [11]. A telescope with arrays of particle detectors would be used to search for discrete sources of gamma-rays, but nothing was found. It was later realized that detecting electromagnetic cascades using Cherenkov radiation would be more sensitive. A telescope consisting of an array of twelve particle detectors looking at Cherenkov radiation was active from 1960-64 but again, no sources were detected. Although the previous experiments failed to make any detections of gamma ray sources, they formed a foundation for further development.

A new method of detecting cosmic gamma rays was developed a few years later at the Lebedev Institute. Cherenkov light is detected using crude mirrors placed in a large telescope to reflect the Cherenkov light onto a detector. This method has remained virtually unchanged since it was first proposed [8]. This technique was first, successfully, applied to gamma-ray astronomy by the Whipple Collaboration starting in 1968. They used a 10m diameter light collector and an array of detectors to record images of the angular distribution of Cherenkov light created by air showers. These distributions would then be used to select out the gamma ray initiated air shower events from among the overwhelming background of cosmic ray initiated events. Twenty years later, in 1989, this technique led to the discovery of the Crab Nebula and effectively started the field of ground-based gamma-ray astronomy [7]. The HEGRA experiment, which followed Whipple, further increased the sensitivity and resolution by using an array of telescopes. Four experiments, MAGIC, HESS, CANGAROO III and VERITAS, launched after the detection of the Crab Nebula.

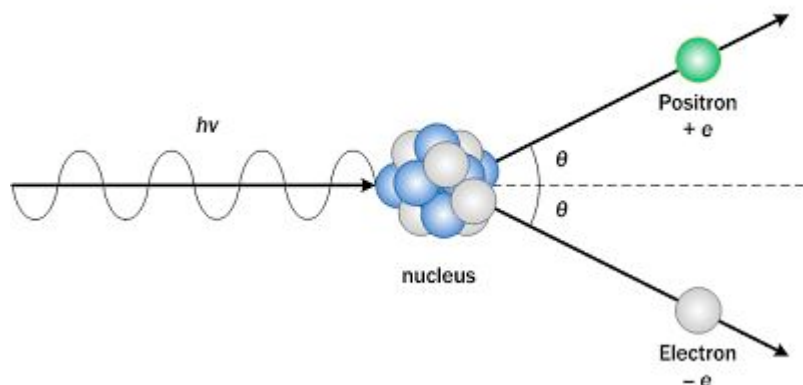


Figure 1.1: Pair Production, *electrons.wikidot.com*

Atmospheric interactions between gamma rays and atmospheric molecules, such as oxygen gas, results in gamma rays being extinguished before reaching sea level. The most common interaction between the gamma rays and molecules in the atmosphere is pair production [11]. When a gamma ray interacts with matter, it is annihilated and the energy goes into producing an electron-positron pair i.e.  $\gamma \rightarrow e^+ + e^-$ . The electron positron pair will have kinetic energy equal to

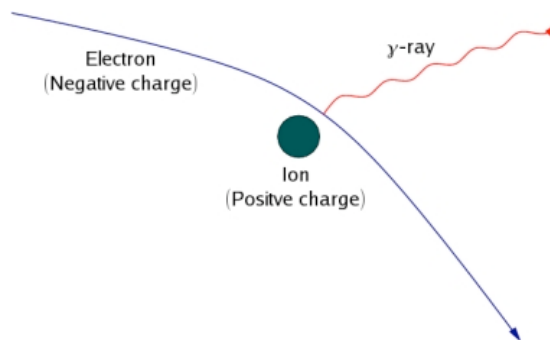


Figure 1.2: Bremsstrahlung Radiation, [www.dur.ac.uk](http://www.dur.ac.uk)

$h\nu - 2M_e c^2$  (Figure 1.1). As the electron pair travels through the atmosphere, additional gamma-rays are created through a process called Bremsstrahlung (Figure 1.2), which occurs when an electron is deflected by the electric field of a nucleus of an air molecule. The new photons may then also undergo pair-production. This results in a cascade of electromagnetic radiation, known as a gamma ray shower, directed towards the Earth as shown in Figure 1.3. If the secondary electrons and positrons in the shower travel faster than the speed of light in the atmosphere, or, in other words, have energy greater than  $m_e c^2 / \sqrt{1 - n^2}$ , where  $n$  is the index of refraction, they will emit additional photons in the UV and optical spectrum through Cherenkov radiation.

### 1.3 Imaging Atmospheric-Cherenkov Telescope

The central difference between ground-based and satellite-base telescopes is the collection area. The typical collection area of a ground-based telescope is on the order of  $10^5 \text{ m}^2$ , roughly 5 orders of magnitude higher than what is achieved with direct detection from satellite based telescopes [12]. Ground based telescopes, however, do not have anti-coincidence shields so a method of rejecting the large background of hadronic cosmic rays is required. In 1977 the technique Atmospheric Cherenkov Imaging, was proposed for this purpose. The basis of this technique is to use telescopes with an array of photomultiplier tubes in the focal plane of large optical reflectors.

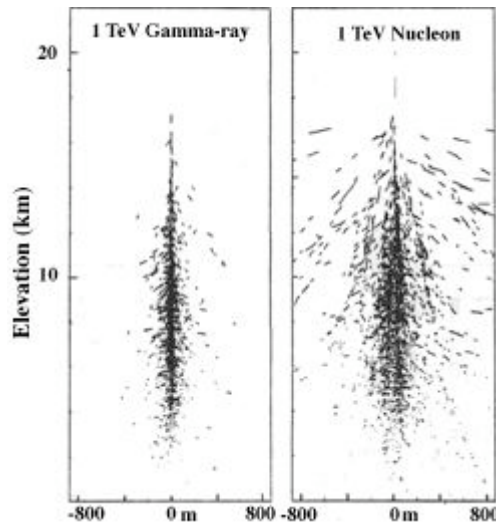


Figure 1.3: Simulations of two Air Cherenkov shower (Left: gamma-ray initiated. Right: Nucleon initiated). The black tracks shows the trajectory of the showers. The horizontal axis shows the spread with respect to the shower axis. *imagine.gsfc.nasa.gov*

This technique exploits a basic difference between gamma-ray initiated showers and hadron showers [12]. The gamma-ray showers have smaller transverse momentum which results in the particle track lengths in gamma-ray showers to be closer to the direction of the primary gamma-ray (Figure 1.3).

The next improvement made was the use to multiple telescopes separated by roughly the same distance as the lateral spread of the shower. A telescope array was shown to have better elimination of local muon background, improved energy and angular resolution, and more accurate measurements of the shower axis location and shower maximum [12]. Muon showers have less radial spread, therefore by requiring multiple telescopes to record an event, the muon background can be significantly filtered. This allow trigger thresholds to be lower. Trigger thresholds determines how low the energy threshold will be. The most important advantage of IACT (Imaging Atmospheric Cherenkov Telescope) over other gamma-ray telescopes is the precision with which the properties of primary gamma-rays can be reconstructed. The yield of Cherenkov light is proportional to the track length of all particles in the shower. The energy of the particles determines the track length, therefore, an image of the shower provides a pseudo-calorimetric measurement of the shower [7].

## 1.4 Purpose of the Research

The research for this paper is aimed at characterizing a potential candidate for a photomultiplier tube to be used in the upcoming CTA (Cherenkov Telescope Array) project. The CTA is a collaboration between the VERITAS, HESS and MAGIC groups, as well as others, to build the next generation ground-based very high energy gamma-ray instruments. Initially, the research was done in preparation for the AGIS (Advance Gamma Ray Imaging System), but has since then merged with several other European groups (MAGIC, HESS) to form CTA. AGIS was to use a new IACT design different from that in VERITAS. The observatory will consist of a large array of different telescopes and the US groups are advocating 36 telescopes with this new IACT design. Construction for the 36 telescopes is expected to start in 2015.

## 2 Experimental Set-up and Equipment

### 2.1 Photomultiplier Tubes

A photomultiplier tube is a device capable to detecting single photons. Photomultiplier tubes have very fast response times which makes them ideal for detecting Cherenkov radiation for particle showers. An electric pulse generated by a PMT is typically a few nanoseconds wide and is produced 20 - 50 ns after illumination[4]. A photomultiplier tube is a vacuum tube with an input window, a photocathode, a dynode chain, and an anode as can be seen in the cross sectional view of a PMT in Figure 2.1. When a photon passes through the transparent input window and hits the photocathode, a photoelectron is sometimes produced through the photoelectric effect and is released into the vacuum. When an electric field is applied, the electron will be accelerated and guided by the electrode to the first dynode. When the electron hits the dynode, a cascade of secondary electrons is produced. This effect continues down the chain of multiple dynodes to create an avalanche of electrons which is collected by the anode and an electronic signal is produced.

For a photoelectron to be produced, the photocathode must be excited by a photon with sufficient energy. Most photocathodes are made of a compound of semiconductor consisting of alkali metals[5]. The semiconductor band theory can be used to describe how the photocathode works. In the band model, there is a band of forbidden energy states called the band gap,  $E_g$ . The work function is the difference in energy between the Fermi level and the vacuum level (Figure 2.2). When an electron in the valance band of the photocathode absorbs a photon with energy  $E \geq E_g$ ,

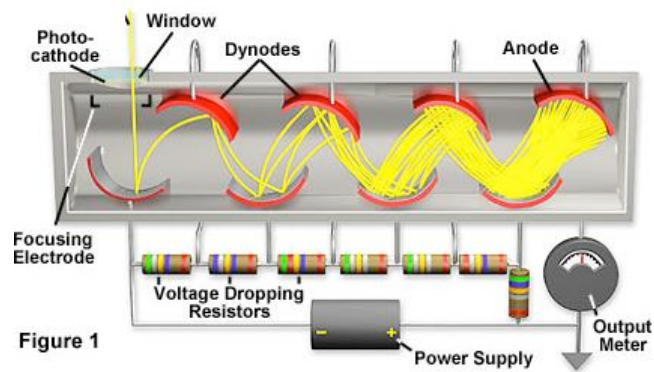


Figure 2.1: Cross section of a photomultiplier tube, <http://micro.magnet.fsu.edu>

it will become excited and move up into the conduction band. Here, the electron will begin to diffuse towards the surface of the photocathode. During this process, the electron will lose energy to electron-electron interactions and interactions with phonons. If the electron has sufficient energy to overcome the vacuum level barrier, it will be emitted as a photoelectron [5]. Semiconductors with low work functions are used as photocathode material to insure that photons up to the infrared range will produce a photoelectron.

The dynode chain is typically constructed from more than ten stages of secondary-emissive electrodes with curved surfaces. Dynodes are typically made of bialkali antimonide and are coated with materials such as nickel, stainless steel or copper-beryllium [5]. If the construction of the dynode is optimal, the energy deposited by the incident photoelectron can result in reemission of multiple electrons from the same surface. Emission from dynodes is similar to the emission from the photocathode; except for the fact that the energy is provided by an electron. The kinetic energy of an electron emitted from the photocathode is on the order of a few eVs. Therefore the energy absorbed by the dynode mainly comes from the acceleration of an electron through a potential difference of a few hundred volts [4]. The structures of the dynode chain can vary the gain, response time and linearity depending on the number of dynodes, layout and other factors.

The anode is an electrode that collects the secondary electrons from the dynode chain,



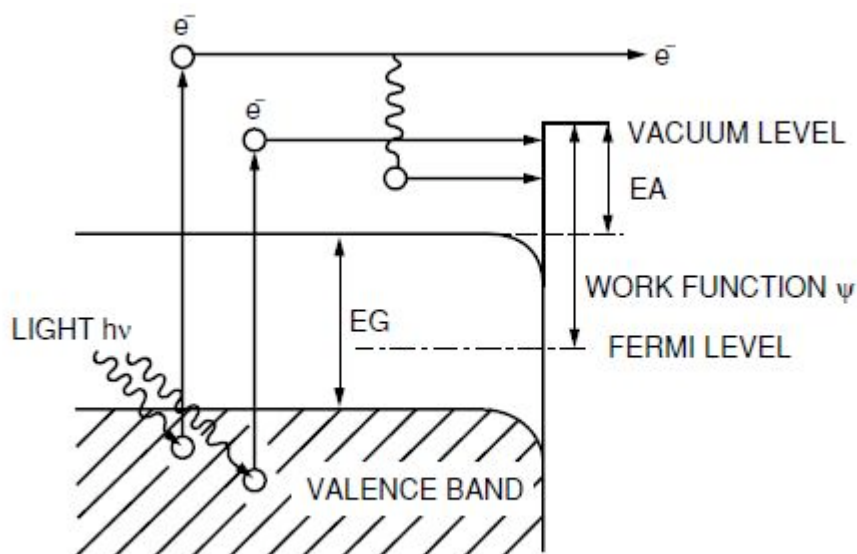


Figure 2.2: Band model for semiconductors[5].

outputs an electron current to an external circuit and generates an electronic pulse indicating the detection of photons.

### 2.1.1 Hamamatsu H8500D-103 MOD 8

Currently we are testing the Hamamatsu H8500D-103 MOD 8 multianode photomultiplier tube (Figure 2.3). The tube we are testing is a modified version of the H8500D-103. It has been modified to have 8 dynode stages instead of 12. Hamamatsu Photonics has recently added this model to its catalogue as the H10966D-103. This particular model has a bialkali photocathode and UV transparent glass. It has 64 pixels each with its own, anode and dynode chain consisting of 8 stages. Each pixel operates similarly to a individual single anode PMT.



Figure 2.3: Hamamatsu H8500D-103 MOD 8. <http://sales.hamamatsu.com>

## 2.2 Electronics and Data Acquisition

The photomultiplier tubes are tested in a light-tight aluminum box to limit the amount of light the photomultiplier tubes are exposed to and standard LEDs are used to illuminate the PMT. Since the signal generated by the PMT is only a few mVs, electronic amplification is used to enhance the signal. The signal is then collected using a DRS4 evaluation board waveform sampler and digital CAMAC scalars.

### 2.2.1 Amplification

Two electronic amplifiers are used to amplify the signal. The first amplifier is a Mini-Circuits pre-amplifier with an electronic gain of approximately 25 . The second amplifier is an amplification system developed at UC Davis for the STACEE experiment. This system has a pre-amplifier and a main amplifier. This system also has an electronic gain of approximately 45. The total amplification is adjusted using electronic attenuators.

### 2.2.2 DRS4 Evaluation Board

The DRS4 evaluation board is a four-channel, 10 gigasample/second waveform sampler. The DRS4 chip was designed at the Paul Scherrer Institute, Switzerland by Stefan Ritt and Roberto Dinapoli. The chip is a switched capacitor array (SCA) capable of digitizing eight channels at sampling speeds up to 5 GSPS. The evaluation board has SMA connectors for four input channels, a USB 2.0 connector and a Lemo trigger input. The board is powered through the USB port and contains on-board trigger logic[10]. For the purposes of this experiment, only two channels are used. One channel is used to sample the output signal of the PMT and the other channel is used for a gate to act as a trigger to align the timing of the PMT signal and the flashes of the LED.

### 2.2.3 CAMAC

A Computer Automated Measurement and Control (CAMAC) crate is a standard bus for data acquisition. The crate allows for data transfer between various plug-in modules. A crate controller is used to interface with a PC using GPIB (General Purpose Interface Bus). The two primary modules used for this experiment are the LeCroy 2551 12 Channel 100 Mhz Scaler and the LeCroy 4413 16 Channel Programmable Discriminator.

A discriminator is used to filter out signals below a specified voltage threshold. The discriminator module will output a signal every time it reads a signal larger than the specified voltage. The output of the LeCroy 4413 is an ECL signal and a LeCroy 616 16-Channel ECL/NIM/ECL Converter is used to convert the signal to a NIM signal. The 16 channels of the LeCroy 4413 all share a common threshold which is set using CAMAC commands on the PC.

The LeCroy 2551 scaler reads in a NIM signal and counts the number of input signals at a rate of up to 100 MHz. The module contains 12 channels, each with 24 binary bits. Up to  $1.6 \times 10^7$  counts can be read before the scaler needs to be cleared. The output of the scaler is read using CAMAC commands on the PC.

## 3 Experimental Procedure and Software

Programs based in C++ and the ROOT graphical interface are used to acquire and analyze the data. ROOT is an object-oriented program and library developed by CERN for the purposes of data acquisition and analysis in high-energy physics. ROOT uses the CINT compiler to allow C++ scripts to be used in ROOT macros and ROOT libraries to be used in stand alone C++ programs.

### 3.1 Gain Measurement

The gain is the amplification of a signal photoelectron pulse. The total PMT gain is determined by the applied voltage, and the structure of the dynode chain. Photoelectrons emitted are multiplied by a factor ranging from 10 to  $10^8$ , depending on the applied bias and structure of the dynode.[5]. The secondary electron yield from the dynode is a sensitive function of the applied voltage. The overall gain is

$$\text{gain} = \alpha \times \delta^n$$

where n is the number of dynodes,  $\alpha$  is the fraction of all photoelectrons collected by the dynode structure, which is determined by the structure and composition of the dynode, and  $\delta$  is the overall multiplication factor on a single dynode [4].

$$\delta = a \times E^k$$

where a and k are constants determined by the material and structure of the dynode. E is the interstage voltage of the dynodes.

Gamma ray telescopes use several hundred PMTs and it is important for all the PMTs to

have the same behavior, therefore it is important that the gain is the same for all tubes. Gain measurements are usually the first measurements to be done for this reason. We normally operate all PMTs at a gain of  $2e5$  but not all PMTs operate at the same applied bias. The gain is very sensitive to the structure of the dynode and each individual tube of the same model will generally yield slightly different gains for the same applied bias, therefore it is important to characterize the gain of a PMT in order to calibrate the system so that all PMTs yield consistent results.

### 3.1.1 Procedure

The gain of a PMT is the amplification of a single photoelectron within the dynode chain. This is measured by integrating the output signal generated by the anode. The integration will determine the total charge in the signal and thus the gain can be found by dividing the charge of an electron. For this method to work, it is necessary to ensure that the signal contains only one photoelectron; that is, only one photon is detected at a time. To accomplish this, we use a Phillips PM 5712 pulse generator to flash an LED at a rate of 4kHz. The LED is then attenuated by a factor of 1000 using an optical filter and focused into an optical fiber. The position of the fiber is then placed in front of the PMT at a distance such that the amount of light detected by the PMT is approximately one every twenty flashes. This 5% light level has a 99% confidence that only one photon will be detected per signal. To ensure that the photons detected only originated from the LED, a gate signal is used. The gate signal is produced by using the same signal from Phillips pulse generator to create a 100ns gate using the output of a LeCroy 623B discriminator module. The gate signal is also used to trigger the oscilloscope and DRS. Each time a gate is generated, the LED is flashed once. To match the timing of the gate with the PMT signals, the gate is delayed by 100ns by using a 100ns cable. This gate signal is used as the trigger for the DRS. In the analysis, the PMT signal must coincide with this 100ns gate to be recognized as a valid signal. All other signals, from light leaks or thermal fluctuations are ignored. Figure 3.1 shows the circuit used for this experiment. The signal of the PMT must be amplified using a combination of

the STACEE amplifier, Mini-Circuits preamplifier and attenuators. The PMT signal must be large enough to have a good separation between the noise and the single photoelectrons. The tail end of the distribution of single photoelectron amplitudes can extend out to about five to six times the single photoelectron amplitude. The DRS only has a range of up to 900mV. We found that a single photoelectron amplitude of approximately 100mV will be sufficiently large for separation of noise and small enough so that the tail end of the distribution will not be lost. With the right combination of amplifiers and attenuators, the resulting single photoelectron amplitude is around 100mV.

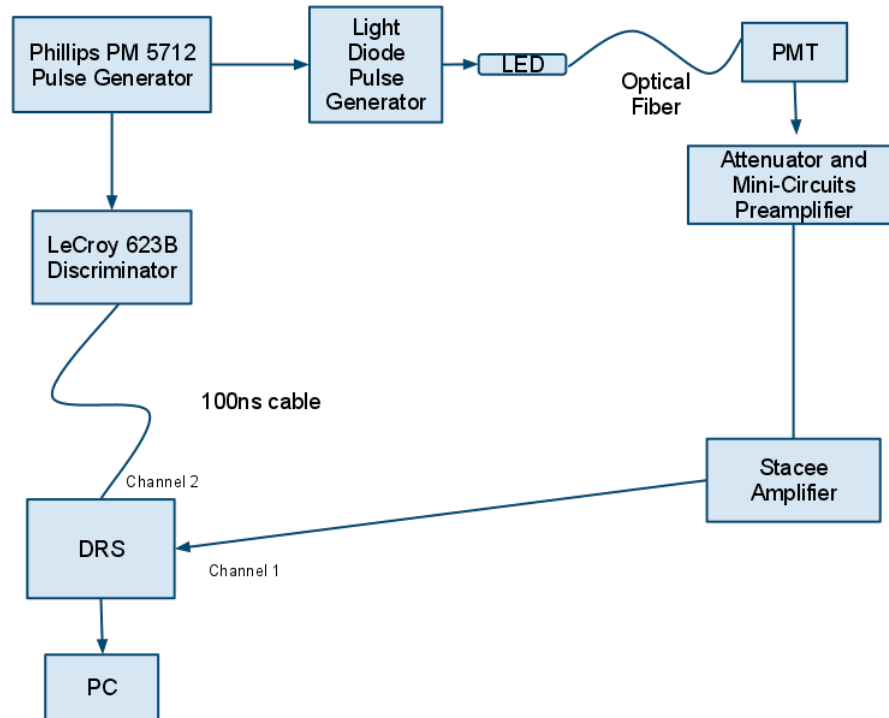


Figure 3.1: Circuit diagram used in the gain measurements.

### 3.1.2 Software

Two programs are used to make this measurement. A stand alone C++ program used to interface with the DRS is used to record the PMT signal. A ROOT macro is used to analyse the resulting data.

The program to interface with the DRS is found in the directory, */root/Desktop/DRS*. The source code is found in *DRS/src*. To run the program, the command *./drs\_gui* is used. This command will prompt the graphical user interface as shown in Figure 3.2 to appear if the DRS is plugged in.

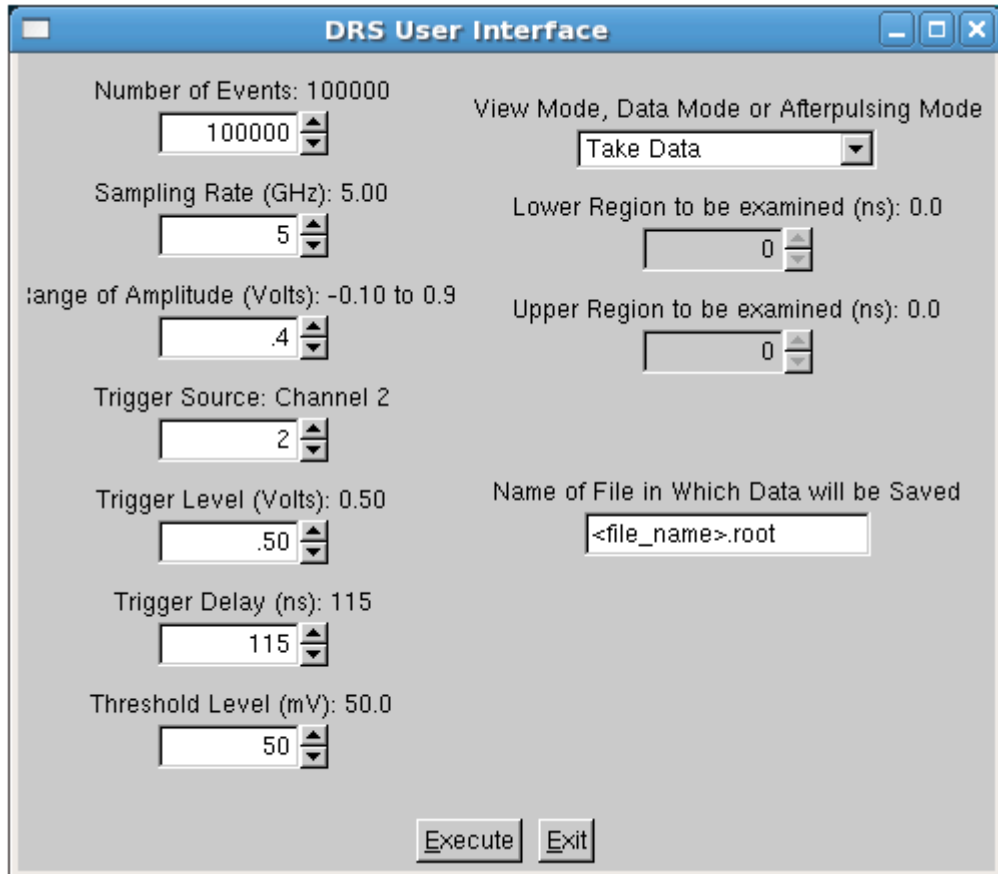


Figure 3.2: Graphical user interface used to control the DRS .

The number of events option is the number of triggers the user wishes to record or analyse. The sampling rate option defines how fine the data points will be. For each event, the DRS board can only take 1024 data points. At the maximum sampling rate of 5 GHz, the DRS can record or analyze a 204 ns window. The DRS has a 1V range, the range of amplitude option will set the midpoint of this 1V range. The trigger source option determines which channel the DRS will trigger

on. In this experiment, the trigger source is the gate which is plugged into channel 2. The trigger level option sets the trigger threshold for the trigger. The trigger delay option is used to adjust the timing of the trigger. This is used to adjust where in the time window the trigger signal appears. In the analysis, a peak is found by finding a maximum point defined to be such that the points before and after the maximum have a lower value. The threshold level option determines what the DRS will record as a pulse from the PMT and what is just noise; this adds another criteria to filter out the baseline noise. The DRS currently has three working modes, view, take data, check light level. The view mode works very much like an oscilloscope. In a separate window, it will show the signal from the different channels in real time. This can be used to adjust the timing of the trigger delay or to look at the signal to find any anomalies. The check light level mode is used to adjust the light level to 5%. In this mode, the program will analyze the PMT signal on the fly and look for any maxima with amplitude higher than the threshold level. When finished, it will output the number of pulses found and give the light level defined to be the number of pulses divided by the number of LED flashes. In the take data mode, the program will extract the raw traces from the DRS and save them in a root file named by the user in the “Name of file in which Data will be Saved” window.

Gain measurements are done with the default settings on the DRS GUI. The only inputs that are changed are the number of events, the threshold level and name of file. The threshold level is set above the baseline noise determined by looking at the signal on an oscilloscope. The number of events is typically 100,000 for data taking. When adjusting the light level, we only look at a couple thousand events. When the program has finished taking the data, the root file will be saved in the directory, *DRS/Data*.

To analyze the data, the data file is transferred to the vhe2 server. This is done because each root file containing 100,000 events is approximately 850 MB. We wish to save the data file for future reference. Doing the analysis on a separate server also allows us to acquire and analyze data at the same time without slowdown. The data files are saved in the directory, */data\_disks/vhe2b/DRS* and the analysis macro, *Gainmeasure.C* is found in the directory, */data\_disks/vhe2a/DRS*. To



analyze the data, the file name is inputted in the TFile command and the right amplification factor is inputted in the AmpGain variable. The macro will extract the data and generate a histogram of the maximum amplitude of each trace. Since the light level is at 5%, most traces will only contain noise. Therefore the histogram should show two peaks, one peak for the noise and one for the single PE amplitude as can be seen in Figure 4.2. Two Gaussian functions are then fitted to the histogram data. The first Gaussian fits the noise distribution and the second Gaussian fits the single photoelectron distribution. The single photoelectron amplitude is defined to be the mean of the second Gaussian. For a few measurements, the single PE amplitude distribution is very broad and did not have a well defined mean. In this case the Gaussian tries to fit the peak position of the Gaussian to be less than or equal to zero. Since we are only interested in the part of the Gaussian corresponding to pulse amplitudes greater than zero, the median of the positive values of the second Gaussian is calculated; this in theory should be equivalent to the single PE amplitude for distributions with well defined peaks. The macro will then go back through all the traces and extract out the ones with a pulse with amplitude greater than or equal to the single PE amplitude found in the fit. Every pulse is different in amplitude and time so each of the pulses are normalized to 1 and the aligned in time. The average pulse shape is plotted as seen in Figure 4.1. To calculate the gain, the average pulse is integrated and multiplied by the single PE amplitude. This yields the total charge in the average pulse. The charge is divided by 50 ohms to find the total amplification and the amplification factor of the amplifiers to find the gain of the PMT.

## 3.2 Afterpulsing Measurements

Afterpulses are secondary signals not associated with the detection of photons. These afterpulses can be generated by a number of ways. The first way is that stray gas in the vacuum tube can be ionized through interactions with the moving electrons and be accelerated back towards the photocathode. These ions will interact with the photocathode and will typically induce multiple photoelectrons to be produced since the ions will be more energetic than a photon. The photogen-

erated electrons can also sometimes elastically scatter off the first dynode and be redirected back towards the photocathode where more photoelectrons will be produced. Afterpulses can also be produced by optical flashes within the dynode chain, however this process is not well understood. Since these methods involve multiple photoelectrons, afterpulses are typically larger in amplitude than single photoelectron pulses.

### 3.2.1 Procedure

To exploit the fact that afterpulses are larger than single photoelectron pulses, a rate vs threshold curve is used to measure the afterpulsing rate of a photomultiplier tube. A rate vs threshold determines the count rate as a function of pulse amplitude. The signal of the PMT is amplified and sent to the LeCroy 4413 16 Channel Programmable Discriminator (Figure 3.3). The output of the discriminator is converted to a NIM signal and read by the LeCroy 2551 scaler. As the discriminator threshold is increased, smaller pulses will be filtered out, leaving only large amplitude pulses which corresponds to afterpulses. To measure the rate of afterpulsing, we illuminate the PMT with a 450 nm steady LED. The position and voltage of the LED is not important, just as long as the count rate of the PMT is approximately  $1 \times 10^6$  per sec. This base count is found using the discriminator set at the lowest threshold above the noise. This is the base count rate in which we will compare the afterpulsing to. Once the base line is established the count rate of the PMT is recorded using the scaler at several increments of the threshold voltage (Figures 4.4 and 4.5). A second rate vs threshold curve, measurement with all the room lights being turned off is necessary to characterize the dark count rate of the tube. These counts usually originate from thermal fluctuations. The signal of the PMT must be amplified using a combination of the STACEE amplifier, Mini-Circuits preamplifier and attenuators. The LeCroy 4413 discriminator has a minimum threshold of 15mV, so a single photoelectron amplitude to be around 40 mV is desired.

### 3.2.2 Software

The two programs used to make this measurement are `RatevsThreshold.c`, which is a stand alone C++ program used to interface with the CAMAC and acquire data, and `RateCurve.C` which is a ROOT macro used to analyze the data. The `RatevsThreshold` program is found in the directory, `/root/Desktop/CAMAC/Rate_vs_Threshold`. The increment and range of the threshold can be changed if necessary in the `RatevsThreshold.c` file and the time over which each data point is taken can be changed in the file, `data_functions`. The command “`g++ ‘root-config - -cflags - -glibs‘ -lgpibapi -Wno-deprecated -o RatevsThreshold RatevsThreshold.c`” is used to compile the code. The command is `./RatevsThreshold` is used to run the program. When the `./RatevsThreshold` command is given, the computer will search for, initialize and clear the data on the CAMAC controller. It will then initialize the discriminator and set the threshold to its minimum value, 15mV. The system will then sleep for the specified time while the scaler is reading in the data. The number of counts is saved into an array and the count rate is found by dividing the counts by the sleep time and is saved into a separate array. The program then increases the threshold and the process loops until the maximum threshold of 1 V is reached. At each increment, the program will output the current threshold, the number of counts and the count rate. At the end, a plot of the count rate vs the threshold is generated. It is necessary to save the plot as a root file and named in such a way as to distinguish between dark and LED illuminated curves.

Once the two root files are generated, one containing the rate vs threshold curve done in the dark and one containing the rate vs threshold curve done with LED illumination, are generated, the file `RateCurve.C` is used to analyze the data. The name of the root files must be manually input to the code. The `RateCurve.C` file is found in the directory,

`/root/Desktop/CAMAC/Rate_vs_Threshold/RateVsThresholdCurve`.

At the top of the file, there are two commands, `TFile LED(file_name)` and `TFile Dark(file_name)` where the name of the input root files are specified. To run this macro, root must be initialized then the command is `.x RateCurve.C`. The macro will extract the data points from each of the curves

and generate a new rate vs threshold curve with the dark count rate subtracted from the LED flashed count rate. This new rate curve is fitted to a Gaussian function for the single photoelectron distribution and an exponentially decaying tail for the afterpulse distribution. It is defined to be,

$$E \times \left( e^{\frac{A+Bx}{C}} + \frac{1}{2} \times \left( 1 + \operatorname{Erf}\left(\frac{-x+C}{D\sqrt{2}}\right) \right) \right)$$

where A, B, C, D, E are fitting parameters.

The final output will be a fitted rate vs threshold curve with a text box showing the single photoelectron amplitude, parameter C, value along with the afterpulsing rate at 5 PEs or greater, defined to be  $e^{\frac{A+B(5C)}{C}}$  (Figure 4.6).

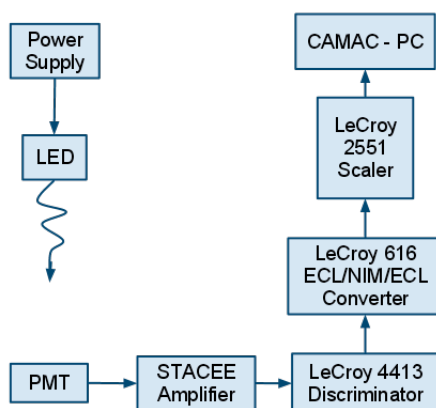


Figure 3.3: Circuit diagram used in the rate vs threshold measurements.

### 3.3 An Alternate Afterpulsing Method

An alternate method of measuring the afterpulsing involves using the DRS to analyze each individual trace and count the number of afterpulses. The circuit used to make measurements is shown in Figure 3.4. The circuit is the same one used in the gain measurements with the addition of a trigger signal generated by another LeCroy 623B discriminator triggered by the pulse generator. This trigger is used to create a 1400 ns window to observe the signal of the PMT. Depending

on the dynode structure, the timing of the afterpulse can range from a few nanoseconds to a few microseconds. Similar to the gain measurement, a pulse generator is used to flash the LED and generate a 100 ns gate. From the default DRS GUI settings (Figure 3.2), the sampling rate is lowered to 0.7 GHz, the trigger source changed to channel 3, and the delay changed to -110 ns. A sampling rate of 0.7 GHz will increase the time window per trigger to 1400 ns. Triggering on channel 3, which is the added trigger signal, and setting the delay to -110 ns will position the gate and PMT signal at the start of the 1400 ns window. This allows the DRS to identify afterpulses up to approximately  $1 \mu\text{s}$  after the initial signal. The analysis to find the PE signals and afterpulses is done on the fly. A PE signal is defined as a maximum with amplitude higher than the threshold level that falls within the 100 ns gate. An afterpulse is defined as a maximum with amplitude higher than the threshold level that appears at least 5 ns after an identified single PE signal.

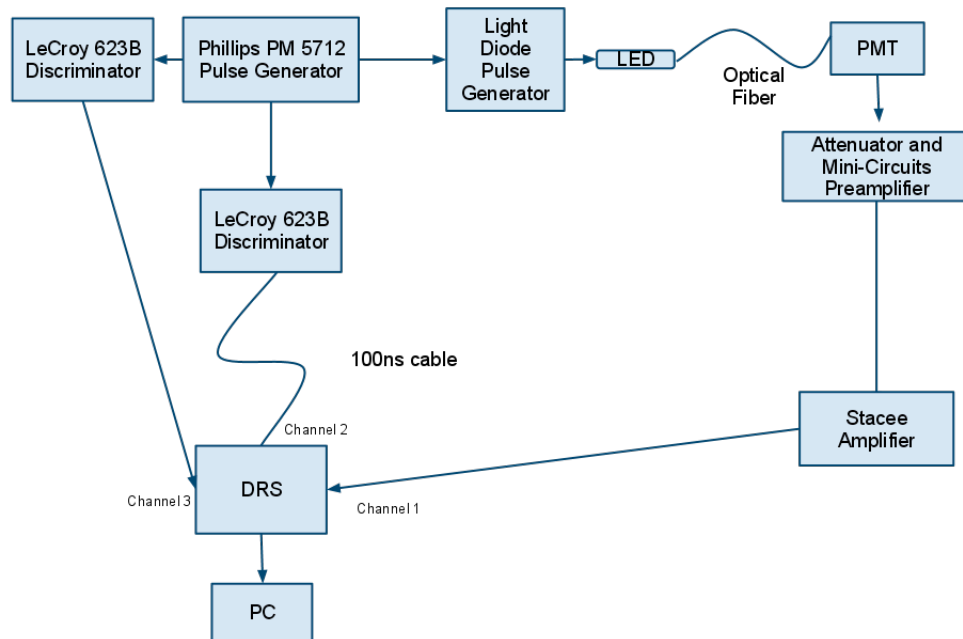


Figure 3.4: Circuit diagram used in the DRS afterpulsing measurements.

When the DRS has analyzed the specified number of events, the program outputs the number of single PE signals and afterpulses found, as well as three histograms. One histogram

shows the distribution of single PE amplitudes found and the another shows the time between an afterpulse and the initial PE signal (Figure 3.5). The DRS is limited to a 1400 ns window so the histogram with the times of the afterpulses is used to check that only a small percent of afterpulses appear after 1400 ns. Since we are interested in afterpulses with 5 PE or higher, the single PE amplitude is determined using the distribution. The third histogram output is a 2D histogram, shown in Figure 3.6, which shows the time and amplitude of all afterpulses found. Using the `OptStat()` function in ROOT, the number of counts with amplitude greater than 5 PE can be found. Using this number, the afterpulsing probability can be found by comparing it to the number of PE signals found.

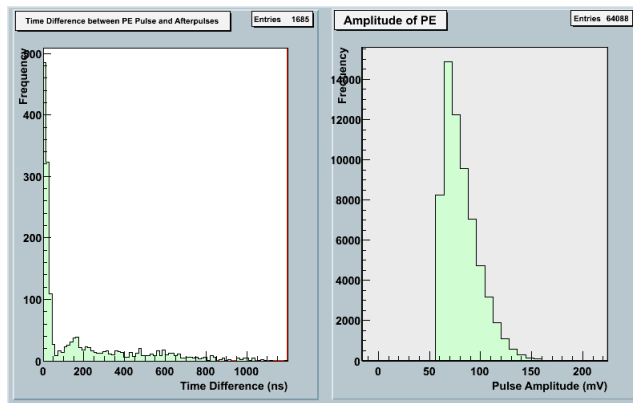


Figure 3.5: Two histograms output by the DRS analysis for afterpulsing. On the left, the time between the initial signal and the afterpulse is shown and on the right, the distribution of single PE amplitudes is shown.

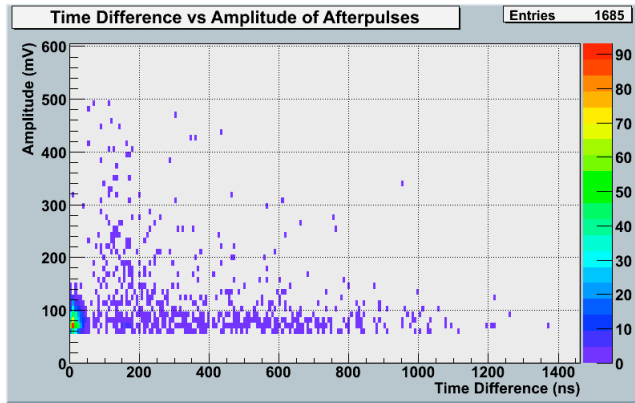


Figure 3.6: A 2D histogram showing the time and amplitude of all afterpulses found.

The figures Figure 3.5 and Figure 3.6 are made using the Hamamatsu H8500D-03. This model has the same design as the H8500D-103 MOD8 with the exception of a different photocathode and a different number of dynodes. The H8500D-03 has a 12 stage dynode chain and the H8500D-103 has been modified to have 8 stages. This method of afterpulsing measurement was not done on the H8500D-103 due to efficiency constraints. Due to the low afterpulsing probability and the requirement of approximately five percent light level, many events must be analyzed to obtain reasonable statistics for the afterpulsing. The histograms shown above (Figure 3.5 and Figure 3.6) were done over seven million events, which took approximately 15 hours and only yielded 15 afterpulses with 5 PE or higher. Because of this, it was not reasonable to use this method for all 64 pixels of the PMT, however we may use this method for a few pixels in the future.

### 3.4 Photon Detection Efficiency

The photon detection efficiency is the probability that a photon incident on the input window will generate a signal. This is determined by the quantum efficiency and collection efficiency of the dynodes, particularly the first dynode.

The quantum efficiency is the probability that an incident photon will induce the photo-

cathode to produce a photoelectron or the number of photoelectons emitted divided by the number of incident photoelectons. When a photon strikes the photocathode, an electron in the valance band will become excited into the conduction band and will begin diffusing towards the photocathode surface. If this electron has enough energy to overcome the vacuum level barrier, then it is emitted as a photoelectron[5]. The quantum efficiency is determined by the materials of the input window and photocathode and can be expressed as [5]

$$\eta(\nu) = (1 - R) \frac{P_\nu}{k} \times \frac{1}{1+1/kL} \times P_s$$

where

R: reflection coefficient of the glass

k: full absorbtion coefficient of photons

$P_\nu$ : probability that light absorbtion may excite electrons to a level greater than then vaccum level

L: mean escape length of excited electrons

$P_s$ : probability that electrons reaching the photocathode surface may be released into the vacuum

$\nu$ : frequency of light

The collection efficiency of the first dynode is defined to be the ratio of the number of electrons landing on the effective area of the dynode to the number of photoelectrons emitted from the photocathode[5]. The effective area of the first dynode is the area of the dynode where electrons can be effectively multiplied by following dynodes without deviating from the most favorable trajectory. Photoelectrons and therefore the signal can be lost before the first dynode if the photoelectrons miss the first dynode.

### 3.4.1 Procedure

To measure the photodetection efficiency, the number of photons incident on the PMT must be known. To do this, a diffuse reflective cylinder and a silicon based PIN diode are used as shown



in Figure 3.7.

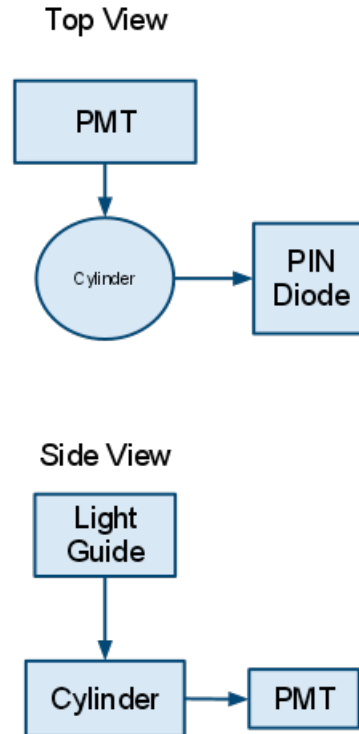


Figure 3.7: LED set-up used to measure photodetection efficiency

The first step is to determine the conversion factor between the number of photoelectrons emitted and the amplitude of the output pulse of the PIN diode. A radioactive Americium-241 source is used to calibrate the PIN diode. Americium-241 alpha decays to Neptunium-237 and the de-excitation of the daughter nucleus produces a 59 keV gamma ray. The silicon in the PIN diode produces one electron-hole pair per 3.62 eV, at room temperature, so the number of photoelectrons per decay can be measured[4]. During a calibration run, the PIN diode is isolated with the  $^{241}\text{Am}$  source. Each time the  $^{241}\text{Am}$  decays, a signal is produced and the conversion factor between the average signal amplitude and number of photoelectrons can be determined. When the PIN diode is exposed to an LED flash, the number of photons incident on the PIN diode can be determined by

analysing the signal amplitude. The quantum efficiency of the PIN diode has been calibrated by the manufacturer (Hamamatsu), so the number photons incident on the PIN diode can be calculated if the number of photoelectrons is known.

The diffuse reflective cylinder has one input for the light source and two arms, one for the test sensor and one for the PIN diode. The cylinder is calibrated by measuring the photocurrent of the same PIN diode situated at two different arms. With this calibration process, the percentage of photons exiting one arm can be calculated relative to the other. The number of counts produced by the PMT is compared to the number of counts produced by the PIN diode. By analysing the amplitude of the PIN diode signal, the number of photons incident upon the PMT window can be calculated.

### 3.4.2 Software

One stand alone executable is used to interface with the CAMAC and modules and a root macro is used to analyze the data. These files are found on MGRODATA5 in the directory, */root/PDE\_Measurement/programming\_file*. The executable, *PDE\_ACQ.exe* reads in data from the LeCroy 2249A 12 Chan ADC and saves the data in a file named *PIN\_and\_TESTSENSOR.root*. This file is to be renamed and copied into the directory */data*. This measurement is done two times, once with the sensors exposed to the LED and once in complete darkness in order to characterize the thermionic noise.

The root macro, *PDE\_Analysis\_Discriminator* is used to analyse the data. The arguments for this macro contain three files: the PMT test data, a calibration file used to determine the conversion factor between PIN signal amplitude and number of photoelectrons and a pedestal file which is the measurement done with no exposure to light. Following the three file name are the wavelength of the LED and a name for the output file. The macro will read in the data from the three files and generate a histogram for the data. The histogram are used to check the data for any anomalies such as increase level of noise. Using the calibration file, the macro will calcu-

late the conversion factor between the signal amplitude and number of photoelectrons. Given the wavelength and data from the PIN diode, the total number of photons incident on the PMT can be calculated using the method described in the previous section. Using the PMT test data, the number of photoelectrons produced by the PMT is measured and the photodetection efficiency is output along with the histograms.

## 4 Analysis and Results

### 4.1 Results of Gain Measurements

The following measurements were made with the Hamamatsu H8500D-103 MOD8 at 890V. The operating voltage was chosen such that the gain of pixel 45 is approximately  $2e5$ . Pixel 45 is the control pixel which the manufacturer used to compare the gain and photodetection efficiency. Figure 4.1 shows a typical average pulse shape and Figure 4.2 shows a distribution of single photoelectron amplitudes for pixel 4 of this particular tube. The measurement was repeated for all 64 pixels. Table 4.1 shows the result of the measurements. The gain of each pixel was plotted to show the distribution of gains as shown in Figure 4.3

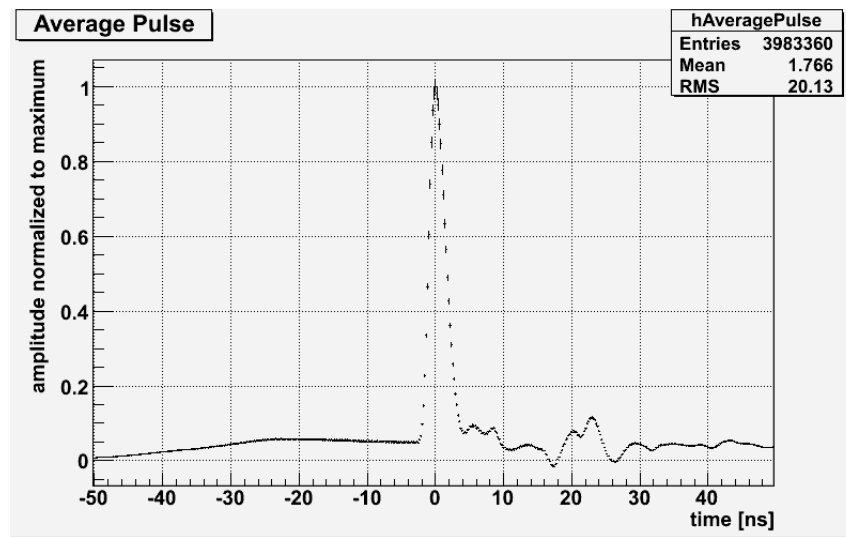


Figure 4.1: Typical average pulse shape for the Hamamatsu H8500D. (pixel 4)

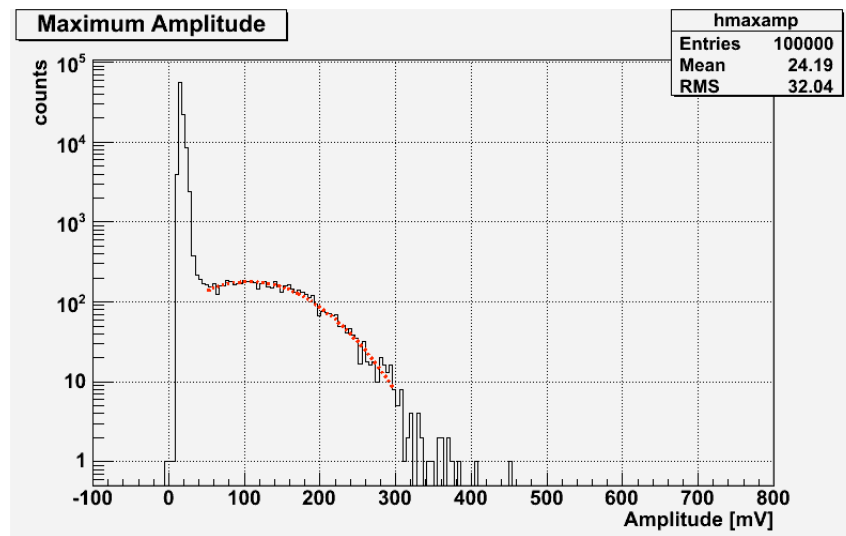


Figure 4.2: Single-photoelectron amplitude distribution for the Hamamatsu H8500D. (pixel 4)

1.44e5	1.77e5	1.89e5	2.19e5	1.75e5	1.69e5	1.70e5	1.91e5
1.42e5	1.76e5	2.12e5	2.06e5	2.06e5	1.82e5	1.45e5	1.75e5
1.34e5	1.74e5	2.19e5	2.33e5	2.20e5	1.76e5	1.55e5	1.72e5
1.33e5	1.62e5	2.02e5	1.91e5	2.08e5	1.87e5	1.73e5	1.79e5
1.38e5	1.54e5	2.14e5	2.07e5	2.24e5	2.05e5	1.86e5	1.71e5
1.36e5	1.66e5	2.04e5	2.32e5	2.17e5	1.98e5	1.62e5	1.64e5
1.37e5	1.68e5	2.26e5	2.48e5	2.37e5	1.83e5	1.42 e5	1.62e5
1.51e5	1.81e5	1.59e5	2.05e5	1.59e5	2.05e5	1.94e5	1.80e5

Table 4.1: Uniformity of the gain rate across the 64 channels.

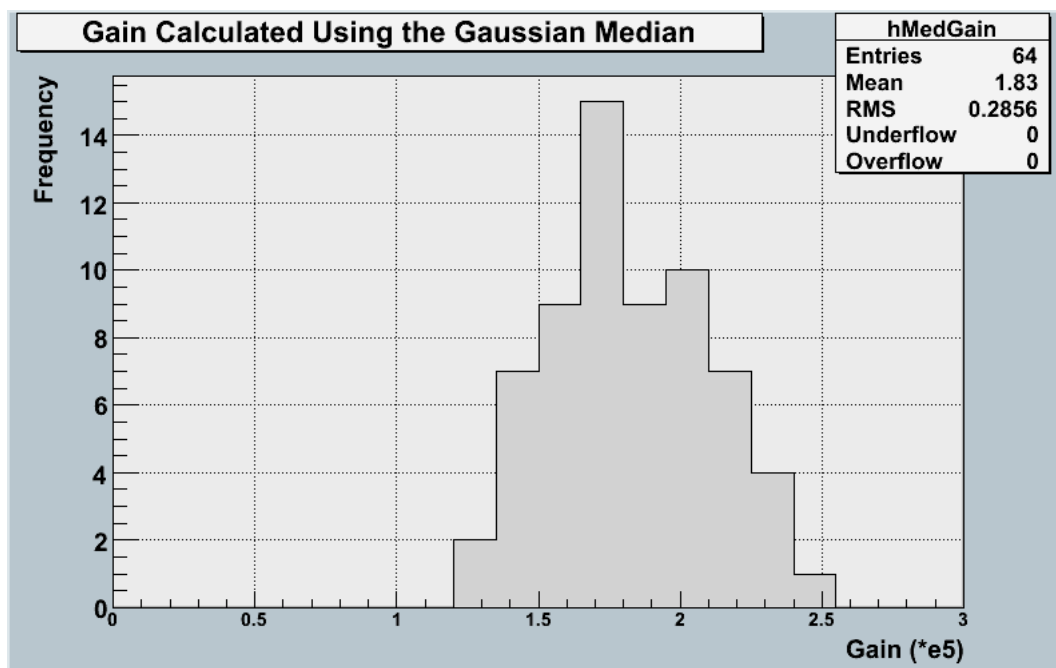


Figure 4.3: Distribution of gains measured for all 64 pixels.

The spread in gain values appear to be acceptable. We observed, however, that the gain of the pixels on the side edges, specifically the left edge, to be significantly lower. We believe this is due to some boundary effects of both the focusing and accelerating electric field. Another possibility is that electrons are being lost when they interact with the sides. If needed, we believe the gain differences can be compensated for by using varying electronic amplification at the cost of complicating the set-up a bit.

## 4.2 Results of Afterpulsing Measurements

The following measurements were made at the same operating voltage as the previous measurement with an electronic amplification of 90. Figures 4.4 and 4.5 shows the results of two rate vs threshold measurements. Figure 4.4 was measured in a completely dark environment and Figure 4.5 was measured by a steady LED. Figure 4.6 shows the rate vs threshold curve with the thermionic noise subtracted out fitted with a Gaussian and exponential function. The measurement was repeated for all 64 pixels. Table 4.2 shows the result of the measurements.

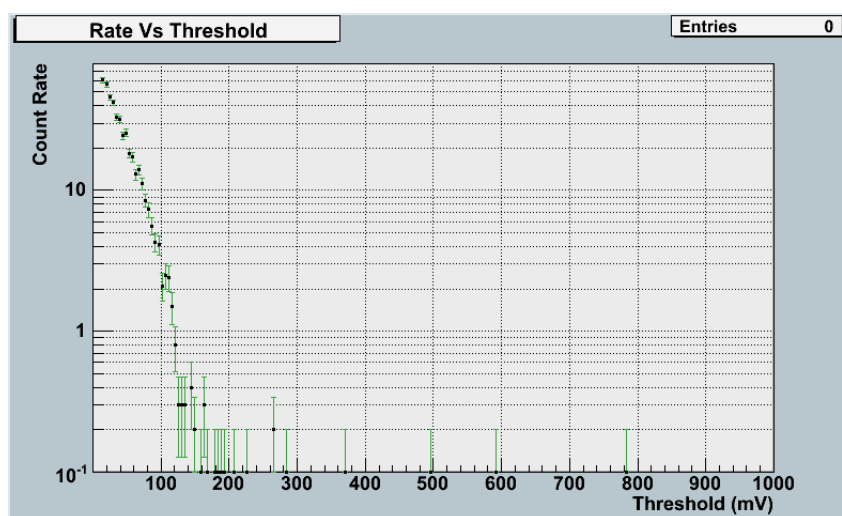


Figure 4.4: Rate vs threshold curve measured in a completely dark environment for pixel 4

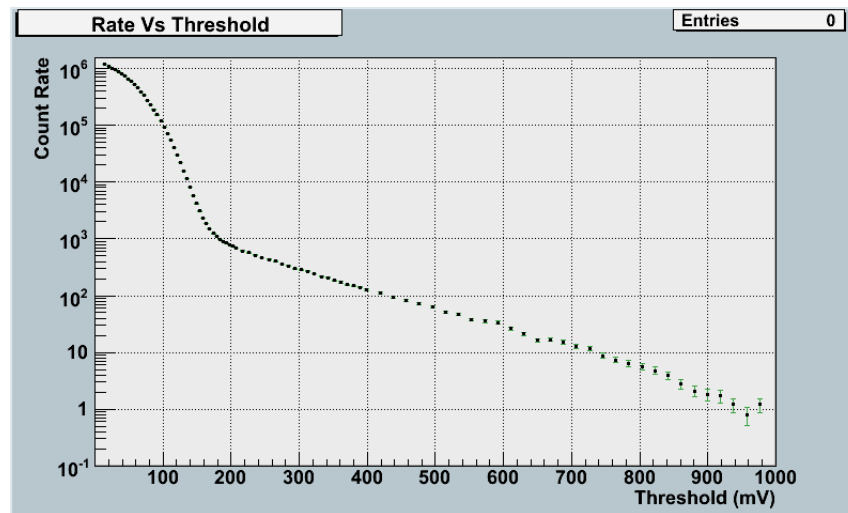


Figure 4.5: Rate vs threshold curve measured with a steady LED for pixel 4

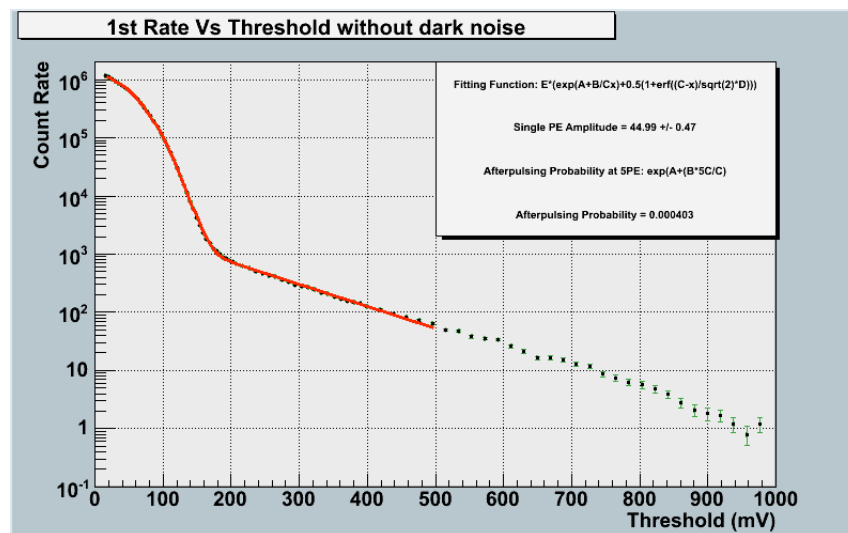


Figure 4.6: Rate vs threshold curve with the thermionic noise subtracted out for pixel 4



9.7e-4	6.5e-4	6.8e-4	6.5e-4	8.6e-4	6.0e-4	4.2e-4	1.2e-3
6.5e-4	1.5e-4	2.9e-4	5.7e-5	5.6e-5	5.8e-5	8.9e-5	1.4e-3
7.8e-4	1.1e-4	4.4e-5	3.7e-5	3.5e-5	3.7e-5	5.7e-5	9.1e-4
1.0e-3	1.1e-4	5.8e-5	2.9e-5	2.8e-5	1.3e-4	4.8e-5	7.3e-4
1.1e-3	1.2e-4	1.1e-2	3.0e-5	2.9e-5	3.1e-5	5.0e-5	6.7e-4
1.2e-3	1.2e-4	4.6e-5	3.3e-5	3.4e-5	5.8e-5	6.1e-5	4.5e-4
1.3e-3	1.5e-4	6.3e-5	1.9e-4	9.5e-5	1.8e-4	1.1e-4	4.4e-4
1.2e-3	4.9e-3	3.5e-4	3.4e-4	5.5e-4	5.6e-4	4.5e-4	5.0e-4

Table 4.2: Afterpulsing rate of the 64 channels. Pixel one is represented by the top left corner.

For the trigger set-up expected to be used in the telescope arrays using the H10966D-103 (Hamamatsu H8500D-103 MOD8), afterpulsing rates of  $1 \times 10^{-3}$  or lower is desired. For many of the pixels, this requirement is satisfied. However, there are a few pixels, specifically the pixels on the edge and corners of the tube, that showed afterpulsing rates a bit higher than the desired level. As mentioned in the previous section, pixels on the side edges and corners typically showed lower gains and behave differently. At this point, it is inconclusive whether or not the high afterpulsing rates are real. There were issues with the data analysis on some of the pixels on the side edges and corners because the single PE distribution was much broader. As shown in Figure 4.7 the single PE distribution is nearly twice as broad as the PE distribution for pixel 4. In Figure 4.7, the single PE amplitude value was not restricted and the analysis returned a negative amplitude. The signal itself does not have a negative amplitude. The issue is that the Gaussian no longer fits well to the data. Similiar to the issue with the broad distribution in the gain measurements, the broad single PE distribution causes the fit to identify a negative amplitude. This issue was observed in several other pixels on the sides, edges, and corners of the tube.

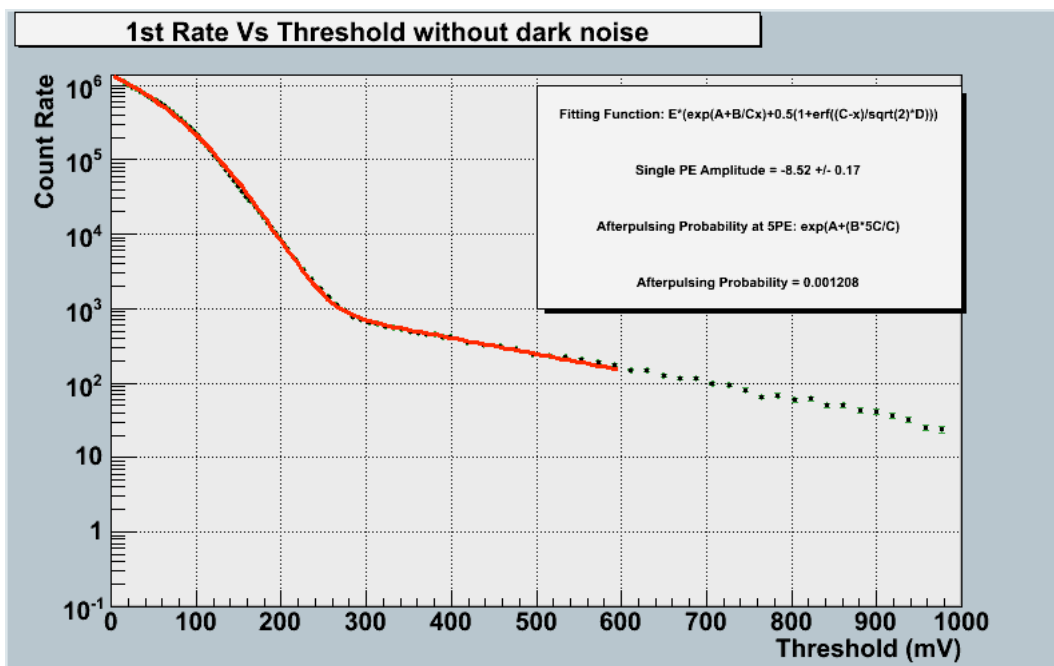


Figure 4.7: Rate vs threshold curve with the thermionic noise subtracted out for pixel 8, a corner pixel

### 4.3 Results of Photon Detection Efficiency Measurements

Although presented in this paper, the following measurements were made by another student[3]. Table 4.3 shows the results of the photon detection efficiency measurements. The measurements were done at an operating voltage of 1000 V with a 450 nm wavelength LED. At this point, the PDE measurements are still incomplete so some pixels have not yet been measured. A PDE value of – was assigned to indicate incomplete pixel measurements.

15.8±0.4	–	16.1±0.4	17.1±0.4	15.6±0.4	–	13.4±0.4	–
–	–	–	19.1±0.5	19.4±0.5	–	–	–
17.3±0.4	–	20±0.5	20.4±0.5	19.1±0.5	–	15±0.4	–
14.9±0.4	16.9±0.4	18.5±0.5	20.5±0.4	20.7±0.5	–	16.5±0.4	17.3±0.4
15.2±0.4	19.3±0.5	18.5±0.5	17.9±0.4	18.5±0.4	17.8±0.4	17.0±0.4	17.0±0.4
–	–	–	21.6±0.5	22.0±0.5	–	–	–
18±0.4	–	20.2±0.5	20.9±0.5	20.0±0.5	–	18.0±0.4	–
–	–	–	19.1±0.5	18.8±0.4	–	–	–

Table 4.3: Photon detection efficiency for various pixels of the H8500D-103 MOD8

The values of the photon detection efficiency are within the typical range for photomultiplier tubes with a bialkali photocathode. The H8500D-103, however, has a super bialkali photocathode so the photon detection efficiency is a bit of a disappointment. As shown in Figure 4.8, a super bialkali photocathode has a quantum efficiency of about 28% at 450nm. This indicates that the collection efficiency is approximately 70%, which is lower than desired. Unfortunately, UBA is not available for this model. So the only way to increase the photon detection efficiency would be to increase the collection efficiency. The collection efficiency is a property of the dynode structure so in order to accomplish this, the dynode structure must be redesigned.

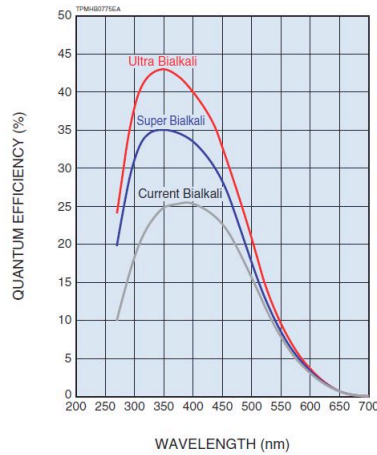


Figure 4.8: Quantum efficiency of three types of photocathodes[6].

## 5 Discussion

### 5.1 Broad Single Photoelectron Distribution

The Hamamatsu H8500D-103 MAPMT shows a much broader distribution of single photoelectron amplitudes when compared to the Hamamatsu R10560 and other models. There are several issues related to this problem. First, it disrupts the measurements of the gain and afterpulsing rates. As show in Figure 4.7 the single photoelectron distribution extends into the 200 mV range, roughly five times higher than the expected value of approximately 40-45 mV. This causes complications in the analysis. The expected fit fails to match the data which causes the analysis to incorrectly calculate the single PE amplitude. The broad distribution also causes the gain analysis program to incorrectly estimate the peak, thus the single photoelectron amplitude, of the distribution. More importantly, the trigger thresholds of the telescope arrays would have to be raised which would increase the energy threshold of gamma-rays that can be detected by the system. Currenty the telescope arrays are planned to have a trigger threshold of about five photoelectrons. Therefore, single photon events from background noise will make spurious contributions to gamma-ray events.

One cause of the spread of single photoelectron amplitudes is the uncertainty in the number of electrons released from the dynodes. The number of electrons released is governed by Poisson statistics. Therefore, there will be an uncertainty of  $\sqrt{n}$  if  $n$  electrons are released by a dynode. By reducing the number dynodes and operating the tube at a higher voltage, the number of electrons released per dynode will increase. This is expected to lower the percentage of uncertainty in the

number of electrons released and thus should reduce the width of the single photoelectron distribution. Figure 5.1 shows the width of the distribution, relative to the single photoelectron amplitude, decreases at higher gains. This measurement was made using the 8 stage H8500-103 MOD8 at higher bias voltages, therefore increasing the number electrons release per stage. We hope to see the same behavior in the same MAPMT with fewer stages.

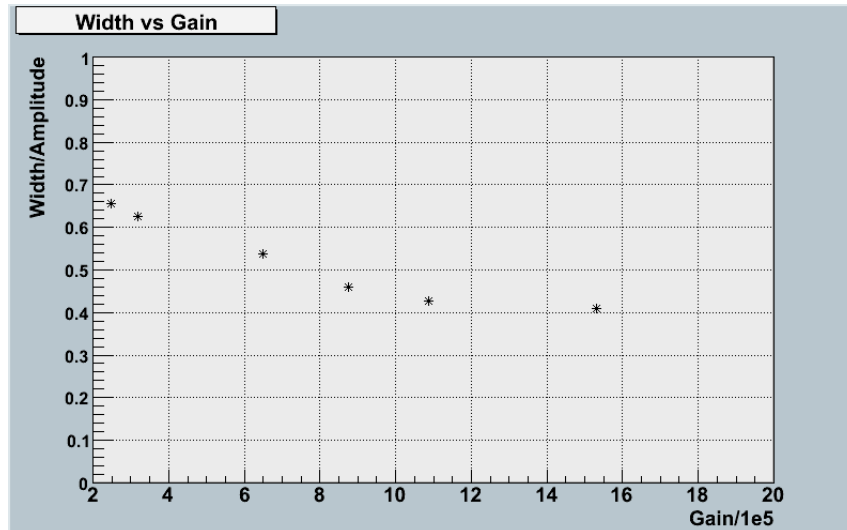


Figure 5.1: Width of the distribution, relative to the single photoelectron amplitude vs gain.

## 5.2 Decrease in Gain at High Light Levels

An issue we encountered during the measurements was that the single photoelectron amplitude does not match between the rate vs threshold and gain measurements. After accounting for the differences in electronic gain, it was found that the single PE amplitude calculated in the rate vs threshold measurements was significantly lower. The rate vs threshold measurements are done by illuminating the PMT with an constant background of approximately  $10^6$  counts per second. The LED is not focused on any one pixel, therefore the tube itself was operating under 64 times the light level of a single pixel. The gain measurements are done with count rates of  $10^4$  and an optical fiber

focused on a single pixel. This led us to believe that the gain sags high light levels. Figure 5.2 shows this behavior.

When the PMT is running, there is a standing current running through the circuit in the base. This circuit is connected to the dynodes and the current provide charge for the electron avalanche. The voltage dropping resistors in the circuit (Figure 2.1) serve two purposes. First, the resistors set up the potential difference between the intermediate dynodes that provides the accelerating and focusing electric field. The second pupose is to limit the amount of current the PMT can draw. If the resistance is too low, then the PMT will draw a lot of power from the power supply and the excess power is lost as heat. If the resistance is too high, then the dynodes cannot draw enough current to maintain the gain at high light levels. We believe this is the cause of the gain sagging. A solution to this problem would be to reduce the resistance. As long as the ratio of resistance is maintained, then the gain of the tube should not change at lower light levels. This simple modification should prevent the gain from saturating at high light levels.

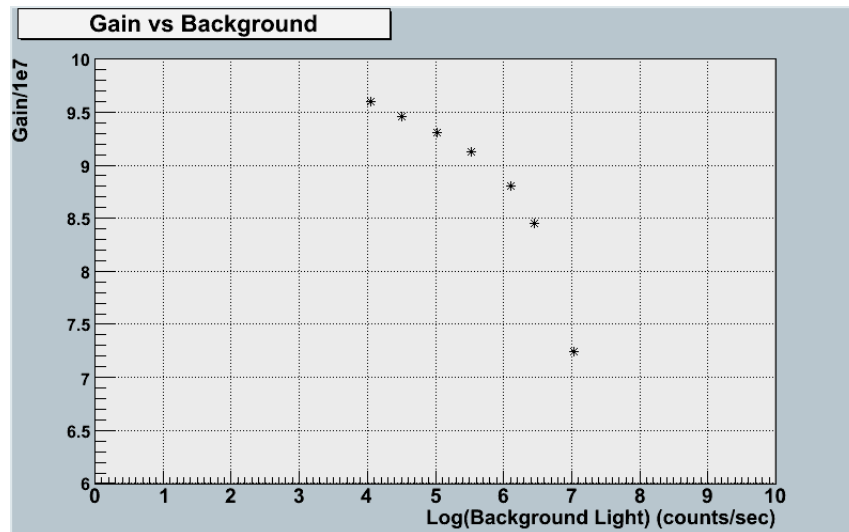


Figure 5.2: Gain of pixel 45 at various background light levels

### 5.3 Conclusion

The decision whether or not to use the H10966D-103 in the upcoming CTA telescopes is still pending on the results of the modification discussed in the previous sections. Hamamatsu is currently working on modifying this model to have six stages instead of eight to address the issue of the broad single PE distribution. This modification may also increase the collection efficiency. We will also want to see what effects changing the resistance in the base will have. One drawback of using fewer stages, however, is that the maximum overall gain is estimated to be  $2 \times 10^4$ , ten times lower than what is currently planned to operate at. Operating the PMT at a lower gain will put higher demands on the electronics since the noise at this gain will be a much more significant contribution to the signal. If CTA is to use this PMT at  $2 \times 10^4$  gain, careful considerations must be made to ensure the noise is minimal. However, operating the PMT at a lower gain does have its advantages. Other telescopes for CTA are currently being planned to operate at  $2 \times 10^4$  gain. Operating a PMT at low gain also has the advantage of being able to operate under brighter night sky background. This means the PMTs do not have to be shut off when facing some particularly bright stars. At this point, however, the Hamamatsu H10966D-103 (H8500D-103) is still the best option.

# Bibliography

- [1] J. Buckley et al. *The Status and future of ground-based TeV gamma-ray astronomy. A White Paper prepared for the Division of Astrophysics of the American Physical Society*, 2008.
- [2] K.S Cheng & Gustavo E. Romero. *Cosmic Gamma-Ray Sources*. Kluwer Academic Publishers, 2004.
- [3] Lloyd Gebremedhin, private communication
- [4] Glenn F. Knoll. *Radiation Detection and Measurement*. John Wiley & Sons, 1989.
- [5] Hamamatsu Photonics. *Photomultiplier Tubes: Basics and Applications*, 3rd edition, 2006
- [6] Hamamatsu Photonics. *SBA UBA Photomultiplier Tube Series*, 1st edition, 2007
- [7] Jim Hilton. *Ground based Gamma-Ray Astronomy with Cherenkov Telescopes*, 2008. New Journal of Physics, 11. URL <http://www.citebase.org/abstract?id=oai:arXiv.org:0803.1609>.
- [8] J. Holder et al. *The first VERITAS telescope*, 2006. Astroparticle Physics, 25, 391.
- [9] Philip Morrison. *On Gamma-ray Astronomy*, 1958. Il Nuovo Cimento, 7, 6: 858865
- [10] Stefen Ritt. *DRS4 Evaluation Board Users Manual*. Paul Scherrer Institute, 2010.
- [11] T.C. Weekes. *Very High Energy Gamma-Ray Astronomy*. Institute of Physics Publishing, 2003.
- [12] T.C. Weekes et al. *VERITAS: the Very Energetic Radiation Imaging Telescope Array System*, 2002. Astroparticle Physics, 17 , 221-243.